Electrostatic Fields Near the Active Site of Human Aldose Reductase: 1. New Inhibitors and Vibrational Stark Effect Measurements†

Lauren J. Webb and Steven G. Boxer*

Department of Chemistry, Stanford University, Stanford, California 94305-5080

Received August 22, 2007; Revised Manuscript Received November 19, 2007

ABSTRACT: Vibrational Stark effect spectroscopy was used to measure electrostatic fields in the hydrophobic region of the active site of human aldose reductase (*h*ALR2). A new *h*ALR2 inhibitor was designed and synthesized that contains a nitrile probe with a Stark tuning rate of 0.77 cm^{-1}/(MV/cm). Mutations to amino acid residues in the vicinity of the nitrile functional group were selected based on electrostatics calculations, possible complications from hydrogen bonds near the nitrile, and comparison with the active site of human aldehyde reductase, whose structure is very similar. Changes in the absorption energy of the nitrile probe when bound to those mutated proteins were then used to quantify perturbations to the protein's electrostatic field. Electrostatic field changes as large as −10 MV/cm were observed. Measured electrostatic fields were compared to predictions based on continuum electrostatics calculations, revealing that substantial modifications to the calculation strategy are necessary. The effects of hydrogen bonding of amino acid side chains to the nitrile probe are considered, and applications of vibrational Stark effect spectroscopy to investigations of ligand binding and biological function are discussed.

The highly organized three-dimensional structure of a protein can support large variations in internal electrostatic fields that influence every aspect of the protein's function (*1*−*3*) including folding (*4*), chemical reactivity and kinetics (*5*−*7*), and protein−protein interactions (*8*). Measurements of the strength and direction of these fields are therefore of great importance, and represent a long-standing biophysical challenge (*9*−*16*). One strategy that has been developed in recent years is vibrational Stark effect (VSE[1]) spectroscopy, which describes the influence of an electric field on a molecular vibrational frequency and can be observed through infrared spectroscopy (*17*, *18*). VSE spectroscopy is a two-step experiment. In the first step, a vibrational probe is selected and the effect of a known external applied electric field on the infrared absorption frequency is used to calibrate sensitivity of the oscillator's vibrational frequency to an electric field. The magnitude of this effect is called the Stark tuning rate, and is taken as an intrinsic property of the oscillator. In the second step, the calibrated vibrational probe is inserted into a protein of interest and used as a highly local, sensitive, and directional reporter of changes of the protein's electrostatic field as perturbations are made to the protein, for example by amino acid mutagenesis. We use the term "vibrational Stark effect" to describe both the effect of a known applied external electric field on an oscillator's vibrational frequency and the absorption frequency shifts in the IR spectrum of the calibrated spectator vibrational probe when it is exposed to a perturbation inside a protein.

Here we introduce an ideal vibrational Stark probe, the nitrile (C≡N) functional group (*19*), into the active site of the protein human aldose reductase (*h*ALR2) through inhibitor binding (*17*). Aldose reductase is a 36 kDa, soluble, monomeric enzyme that reduces aldehydes using the NADPH cofactor and that is believed to be responsible for many of the long-term health consequences of diabetes (*20*−*25*) and so has been the subject of extensive structural and catalytic experiments and calculations (*20*, *26*, *27*). Tight-binding inhibitors of this enzyme have been developed for pharmacological treatment of diabetes (*22*, *24*, *25*, *28*, *29*), and high-quality crystal structures of *h*ALR2 bound to inhibitor molecules have been published (*30*, *31*). One such inhibitor, IDD594 (indexed by the Institute for Diabetes Discovery) (*29*), was recently characterized in a remarkable crystal structure solved to 0.66 Å resolution (*32*), providing high quality structural information on the position of the inhibitor, amino acid residues, and solvent molecules in the active site of the enzyme. The molecular scaffold of this class of inhibitors can be functionalized with a variety of chemical groups and still bind to the active site of *h*ALR2 (*17*, *29*). Given the high binding affinity of these inhibitors, and given the high degree of structural information from crystal structures describing how these inhibitors bind to the active site of *h*ALR2, we have designed an inhibitor (**1**, Figure 1) that binds to *h*ALR2 in an orientation that places a nitrile group into a position of the protein active site far removed from the protein surface, where it is protected from water. A model structure of this inhibitor in the active site of *h*ALR2 was constructed based on the high-resolution crystal struc-

† This work was supported in part by the National Institutes of Health (GM27738). L.J.W. acknowledges the NIH for a NRSA postdoctoral fellowship 1F32GM076833-01.

* E-mail: sboxer@stanford.edu. Phone: (650)723-4482. Fax: (650)-723-4817.

[1] Abbreviations: *h*ALR2, human aldose reductase; VSE, vibrational Stark effect; IR, infrared; IDD, Institute for Diabetes Discovery; FCC, flash column chromatography; DMF, dimethylformamide; DIEA, diisopropylethylamine; MeTHF, 2-methyltetrahydrofuran; PBE, Poisson−Boltzmann equation; MD, molecular dynamics; *h*ALR1, human aldehyde reductase.

10.1021/bi701708u CCC: $40.75
Published on Web 01/19/2008

tures of related inhibitors, IDD594 (*32*) and IDD393 (*31*). This strategy was used successfully for estimating the position of yet another *h*ALR2 inhibitor, IDD743, in the active site of the protein, which has recently been confirmed by a crystal structure (*33*). The model structure for inhibitor **1** is seen in Figure 1, and shows that one phenyl ring of this inhibitor is buried deep in the active site of the enzyme, where crystallography data has confirmed that no water is present (*32*). By placing the nitrile group at the para position of the buried phenyl ring, the location of the C≡N Stark probe while the inhibitor is bound to the active site of the enzyme is unambiguous, in the sense that rotation of the phenyl ring does not affect the nitrile position.

In the work described here, compound **1** was synthesized and then bound to a series of *h*ALR2 enzymes with amino acid mutations in the vicinity of the nitrile group. The choice of which mutations to express and investigate was guided by three strategies: (1) those that were predicted to cause a large change in the enzyme's electrostatic field at the position of the C≡N bond, (2) removal of a possible hydrogen bond between the nitrile probe and a nearby residue, and (3) comparison to the structurally similar protein aldehyde reductase. Changes in the absorption frequency of the C≡N bond in each mutant with respect to the wild-type (WT) protein were then related directly to changes in the protein electrostatic field caused by those amino acid mutations. This study demonstrates the largest observed changes in electrostatic field measured by a completely general VSE probe, rather than more specialized probes of metal-bound CO and NO (*34*, *35*). In subsequent publications, electrostatics data from VSE spectroscopy will be used to test a theoretical strategy in which extensive molecular dynamics simulations are coupled to electrostatics calculations in the context of high-resolution structural data of **1** bound to both WT and mutant *h*ALR2, as well as detailed investigation of electrostatic contributions to biological function of *h*ALR2 and closely related enzymes.

MATERIALS AND METHODS

A. Synthesis of a Nitrile-Containing Inhibitor of hALR2. The nitrile-containing inhibitor of *h*ALR2, (5-chloro-2{[4-cyanobenzyl)amino]carbonyl}phenoxy) acetic acid, **1**, was synthesized according to the procedure described in Scheme 1 (*29*). Unless noted, all starting materials were used without further purification, and all reactions were carried out under an atmosphere of N_2(g). Flash column chromatography (FCC) was carried out with silica gel (Aldrich, 230−400 mesh, 60 Å) equilibrated in heptane. The proton nuclear magnetic resonance spectrum of product **1** was obtained on a 200 MHz Varian Gemini spectrometer.

4-Chloro-2-hydroxybenzoyl Chloride. A slurry of 5.96 g of 4-chloro-2-hydroxybenzoic acid (Aldrich, 93%) in 20 mL of CH_2Cl_2 was prepared, and 50 mL of oxalyl chloride was added dropwise over several minutes. A drop of dimethylformamide (DMF) was added, and the solution was stirred at room temperature for 24 h. Excess oxalyl chloride was removed under vacuum, the solution was filtered, and excess CH_2Cl_2 was removed under vacuum. The acid chloride product was used in the next reaction without further purification.

4-Chloro-N-(4-cyanobenzyl)-2-hydroxybenzamine. The acid chloride starting material was dissolved in 30 mL of CH_2Cl_2 and chilled to 0 °C. Diisopropylethylamine (DIEA, 11 mL) was added dropwise. 6.28 g of 4-(aminomethyl)-benzonitrile hydrochloride (Aldrich, 97%) was added, and the solution was stirred at room temperature for 24 h. The CH_2Cl_2 was then removed under vacuum, and the amide product was extracted with ethyl acetate, washed sequentially with 1−2 M HCl(aq) and saturated NaCl(aq), and dried over $MgSO_4$. The $MgSO_4$ was removed by filtration, excess ethyl acetate was removed under vacuum, and the product was separated and isolated by FCC (product eluted with 20% (v/v) ethyl acetate in heptane). Yellow fractions were combined, and excess solvent was removed under vacuum.

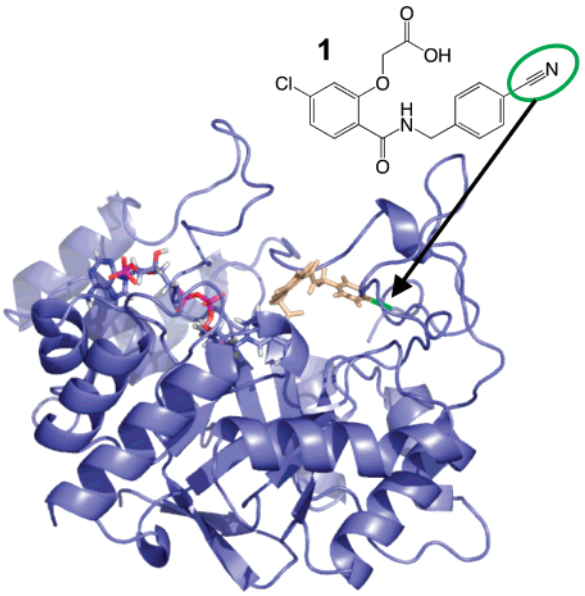

FIGURE 1: Location of bound inhibitor **1** (wheat) and the $NADP^+$ cofactor in WT *h*ALR2. The nitrile functional group is shown in green.

Ethyl (5-Chloro-2{[(4-cyanobenzyl)amino]carbonyl}phenoxy) Acetate. The amide starting material was dissolved in 15 mL of acetone, and 9.5 mL of 2 M K_2CO_3(aq) was added. Ethyl bromoacetate (500 μL) was added, and the solution was heated at 50 °C for 2 h. After returning to room temperature, the solution was cooled to 0 °C and 1 M HCl-(aq) was added until the solution was pH = 1. The product was extracted with ethyl acetate, washed with saturated NaCl-(aq), and dried over $MgSO_4$. The $MgSO_4$ was removed by filtration, and the resulting product was purified by FCC (product was eluted at 20% (v/v), 60% (v/v), and 100% (v/v) ethyl acetate in heptane). Yellow fractions were combined, and excess solvent was removed under vacuum.

*(5-Chloro-2{[(4-cyanobenzyl)amino]carbonyl}phenoxy) Acetic Acid (**1**).* The acetate product from the previous reaction was dissolved in 12 mL of ethanol, and 2 mL of 2 M NaOH-(aq) was added. The solution was stirred at room temperature for 4 h, after which the ethanol was removed under vacuum. 1 M HCl(aq) was added to the solution until pH = 0, resulting in a white precipitate. The precipitate was extracted into ethyl acetate, washed with saturated NaCl(aq), and dried with $MgSO_4$. After removing the $MgSO_4$ by filtration, the ethyl acetate was removed under vacuum. The resulting white powder was washed with CH_3CN and H_2O (neutral pH), and dried. (9.2 ppm, t, 1 H; 7.9 ppm, d, 1 H; 7.8 ppm, d, 2 H; 7.5 ppm, d, 2 H; 7.3 ppm, s, 1 H; 7.2 ppm, d, 1 H; 4.9 ppm, s, 2 H; 4.6 ppm, d, 2 H.) 345 *m*/*z* (ES+), 344.6 calculated.

Scheme 1

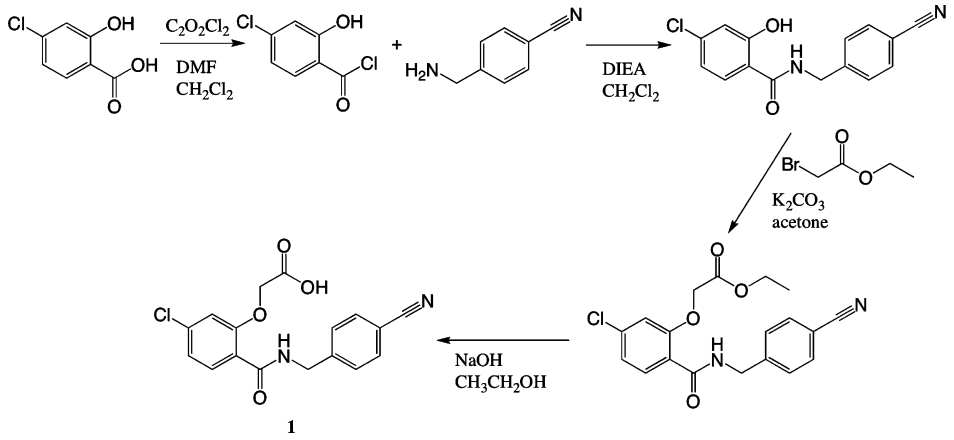

1

B. hALR2 Expression and Purification. The expression and purification of *h*ALR2 was conducted as described previously with several modifications (*17*, *36*). The gene for wild-type (WT) *h*ALR2 was obtained from Dr. Alberto Podjarny in the pET-15b expression vector (Novagen) and sequenced. Amino acid mutations were made using the Quikchange mutagenesis kits (Stratagene) with PCR primers obtained from Elim Biopharmaceuticals, Inc. (Hayward, CA). WT and mutant plasmids were transformed into the *Escherichia coli* strain BL21(DE3) (Novagen) for protein expression. In a 6 L shake flask, 2 L of sterilized LB media with 100 μg/mL ampicillin added were inoculated with the plasmid-containing *E. coli* and grown for approximately 4 h at 37 °C. Expression of *h*ALR2 was then induced with the addition of IPTG to a concentration of 1 mM. After induction, the growth was maintained at 37 °C for approximately 4 h. The cells were then pelleted, resuspended in a lysis buffer of 50 mM phosphate pH = 8, 300 mM NaCl, and 10 mM imidazole, flash frozen, and stored at −20 °C until further use. Isolation and purification of *h*ALR2 from frozen cells was carried out as previously described (*17*). Typical yields were approximately 10 mg of purified protein per liter of growth media. The purity of the final cleaved product was confirmed by SDS−polyacrylamide gel electrophoresis and mass spectrometry.

C. hALR2 Kinetics and Inhibitor Binding. All kinetic measurements were performed with DL-glyceraldehyde as substrate and NADPH as cofactor in 20 mM phosphate pH = 7 buffer at room temperature. Enzyme reaction kinetics were measured by monitoring the decrease in NADPH adsorption at 340 nm over 5 min of at least 2 replicates of each sample. Typical reactions contained 100−200 nM *h*ALR2, 100 μM NADPH, and 5−100 μM DL-glyceraldehyde. Data were fit directly to the Michaelis−Menten equation to determine $k_{cat} = 0.31\ s^{-1}$ for WT *h*ALR2, similar to what has been described before (*26*). The inhibition constant, K_I', of **1** in WT and each mutant of *h*ALR2 was determined under conditions of saturating concentrations of DL-glyceraldehyde and NADPH, and concentration of **1** typically in the range of 0.01−10 μM. The decrease in absorption of NADPH at 340 nm was observed for 5 min, and the slope (V_i) was divided by that obtained with no added inhibitor (V_0). This ratio was fit to eq 1:

$$\frac{V_i}{V_0} = \frac{E - I - K_I' + [(E - I - K_I')^2 + 4EK_I']^{1/2}}{2E} \quad (1)$$

where E is the enzyme concentration, I is the inhibitor concentration, and K_I' is the apparent inhibition constant (*36*, *37*).

D. Continuum Electrostatics Calculations To Predict Protein Electrostatic Fields. A model structure of **1** in *h*ALR2 was constructed from a crystal structure of two similar molecules, IDD594 (*32*) and IDD393 (*31*), as well as the oxidized cofactor $NADP^+$ bonded to WT *h*ALR2 as previously described (*17*). This model was further amended to include the appropriate Cl and C≡N functional groups on the two phenyl rings of **1**. Mutants of interest were constructed in the program PyMol (*38*). In cases where multiple conformations of the mutant amino acid's side chain were possible, several conformers were selected for continuum electrostatics calculations. As described below, these side chain conformations can radically affect the calculated fields, and extensive molecular dynamics (MD) sampling of these conformations may be required to obtain meaningful average values for comparison with the data.

Electrostatic potentials and fields were calculated using DelPhi v.4 (*39*). This program reads in atomic coordinates, charges, and radii and solves the Poisson−Boltzmann equation with the finite difference method (*40*). Charges and radii for protein atoms were taken from the PARSE parameter set, last modified in 1994 (*41*). Inhibitor **1** and the $NADP^+$ cofactor were parametrized with the antechamber package using am1bcc charges in Amber 8 (*42*). Charges from the inhibitor molecule on and near the nitrile bond were expected to dominate the calculation to the extent that they would mask any changes in the electrostatic field of the protein, the value of interest in this study (*17*). To avoid this problem, the carbon and nitrogen atoms of the nitrile and atoms of the phenyl ring within six bonds of the nitrile were left uncharged in the calculation. A focusing strategy was used to balance the needs of accuracy and computation time. An initial calculation that included the entire protein using a coarse grid spacing (0.75 grid $Å^{-1}$, 65 grid lattice) was used to determine the boundary of a subsequent calculation that included only 1/8 of the system with double the grid spacing. This process was repeated three more times to result in a lattice with a grid spacing of 0.167 Å centered on the midpoint of the C≡N bond.

E. VSE Spectroscopy of Inhibitor 1. The sensitivity of the energy of a vibrational transition of the nitrile group, ΔE, to

an electric field was calibrated in an external applied field, $\vec{F}_{Ext}$, according to eq 2:

$$\Delta E = hc\Delta\bar{\nu}_{CN} = -\Delta\vec{\mu}_{CN}\cdot\vec{F}_{Ext} \quad (2)$$

where $\Delta\bar{\nu}_{CN}$ is the change in the absorption frequency of the nitrile vibrational transition and $\Delta\vec{\mu}_{CN}$ is the difference dipole moment of the probe's nitrile bond, also called the Stark tuning rate. A custom sample cell was made of two windows of sapphire coated with 4 nm of Ni separated by 30 μm spacers and attached by copper wires to a high voltage DC power supply (Trek Instruments Inc.) (*19*, *43*). This cell was filled with a solution of 50 mM **1** in 2-methyltetrahydrofuran (MeTHF) and immediately immersed in liquid nitrogen to form a homogeneous frozen glass. Applied fields of ~0.7 MV/cm were synchronized to scans from a Bruker Vertex 70 FTIR with a home-built control unit. Samples were illuminated through a notch filter which transmitted light of 2000−2500 cm^{-1}, and spectra were collected with a liquid nitrogen cooled indium antimonide detector at 1 cm^{-1} resolution. 128 scans with the field applied were alternated with 128 scans with no applied field, and the field-on-minus-field-off difference spectrum was obtained. This spectrum was fit as described previously (*17*, *19*, *43*) to determine a Stark tuning rate, $\Delta\vec{\mu}_{CN}$, of the C≡N probe.

F. Measuring Electrostatic Fields in WT and Mutant hALR2. Solutions of *h*ALR2:**1**:$NADP^+$ of 1:1:2 were equilibrated for ~1 h, then flushed with an excess of 20 mM phosphate pH = 7 in a concentrating centrifuge to a final concentration of ~2 mM. The absorption frequency of the nitrile group on inhibitor **1** was collected at room temperature on the FTIR apparatus described above in a cell made of two sapphire windows separated by Teflon spacers 75−100 μM thick. Spectra were collected with 128 scans at a resolution of 0.5 cm^{-1}. With $\Delta\vec{\mu}_{CN}$ of the probe known, the observed change in absorption energy of the nitrile stretch, $\Delta\bar{\nu}_{obs}$, could be used to determine the change in the electrostatic field of the protein, $\Delta\vec{F}_{protein}$, due to a mutation, from eq 3:

$$\Delta E = hc\Delta\bar{\nu}_{obs} = -\Delta\vec{\mu}_{CN}\cdot\Delta\vec{F}_{protein} \quad (3)$$

with the convention that the probe difference dipole points from the partial positive charge on the carbon atom to the partial negative charge on the nitrogen atom (*17*, *44*). In this convention, $\Delta\vec{\mu}_{CN} < 0$ and the angle between the difference dipole and the coordinate axis is 180°. This convention is explained and discussed in the Appendix. With this definition, a shift in $\Delta\bar{\nu}_{obs}$ to lower energy indicates $\Delta\vec{F}_{protein} < 0$. It is important to note that in this experiment the absolute field of the protein, $\vec{F}_{protein}$, is not defined and cannot be measured directly. Instead, the change in protein field upon making a perturbation such as an amino acid mutation is the observed quantity.

RESULTS AND DISCUSSION

The low temperature absorption and Stark spectra of inhibitor **1** are shown in Figure 2. The magnitude of the Stark tuning rate of the nitrile group in inhibitor **1** was found to be 0.046 D or 0.77 cm^{-1}/(MV/cm), similar to what has been seen previously for nitrile-functionalized phenyl rings (*19*). This Stark tuning rate means that a change in electric field

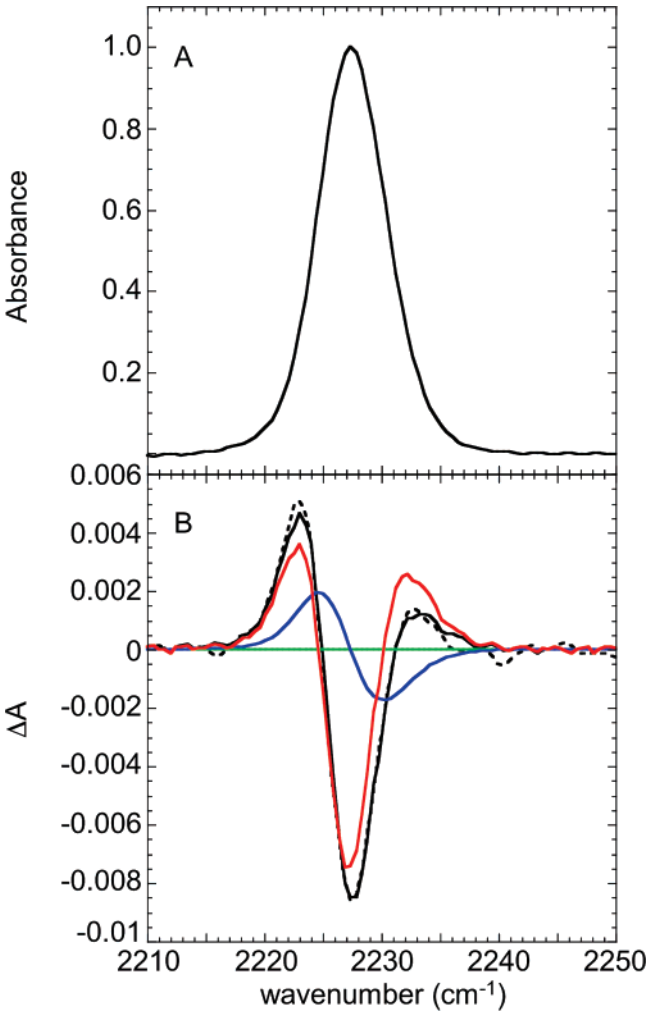

FIGURE 2: Vibrational Stark effect spectrum of inhibitor **1** dissolved in 2-methyltetrahydrofuran (2-MeTHF). (A) Absorption spectrum of **1** at 77 K in the absence of an external applied electrostatic field normalized to an absorbance of **1** (from a measured absorbance of 0.035). (B) Difference spectrum ΔA (field on minus field off) normalized to an applied field of 1 MV/cm (dashed line), contributions from the 0th (green), first (blue), and second (red) derivative to the spectrum, and the overall fit (black). $|\Delta\vec{\mu}_{CN}| = 0.046\ D = 0.77\ cm^{-1}$/(MV/cm).

of +1 MV/cm (i.e., increasing in the direction that a point positive test charge would move if placed in the field) projected onto $\Delta\vec{\mu}_{CN}$ will cause the vibrational energy of the C≡N bond to shift by +0.77 cm^{-1} (see Appendix for sign convention). Given that electrostatic fields in proteins are predicted to range over greater than ±20 MV/cm and the resolution (0.5 cm^{-1}) and sensitivity (>100 S/N) of our FTIR instrument under standard experimental conditions, this molecule is indeed a sensitive probe of a protein's electrostatic environment. Assuming that $\Delta\vec{\mu}_{CN}$ lies along the internuclear axis of the C≡N bond, which has been shown to be the case in the nitrile probes examined to date and is expected for a localized oscillator (*43*), then both the magnitude and the direction of the shift in protein electrostatic field can be measured.

In general the active site of *h*ALR2 proved to be quite robust to mutation. WT *h*ALR2 displayed $k_{cat} = 0.30 \pm 0.06$ s^{-1}, and every mutant discussed here had $k_{cat} > 0.1$ s^{-1}. Inhibitor **1** bound strongly to WT *h*ALR2 and all mutants except T113A/F115Y, with K_I' ranging from 40 nM to 8

μM (compared to 20 nM for IDD743 in WT *h*ALR2). (*45*) The absorption frequency of the nitrile on **1** in buffered solvent was ~2236 cm^{-1}, > 3 cm^{-1} higher than the absorption energy measured in WT or any mutant *h*ALR2 (*vide infra*). The full width at half-height (FWHH) of **1** in buffered solvent was 10 cm^{-1}, but when bound to WT *h*ALR2 decreased to 8 cm^{-1}. Thus line widths and peak positions were clear spectroscopic evidence that the inhibitor remained tightly bound to each enzyme during the course of the experiment.

A primary reason for using the *h*ALR2/IDD-type inhibitor system is the high quality of multiple inhibitor/protein structures available. Three inhibitors, IDD594, IDD393, and IDD388, have been characterized bound to *h*ALR2 with resolution ranging from 0.66 Å to 1.55 Å (*31*, *32*, *46*). These structures show an almost identical conformation of the inhibitor in the active site pocket (RMSD ≤1.7 Å of the inhibitor heavy atom scaffold). The binding interactions for the IDD-type scaffold have been shown to be due to the hydrophobic pi stacking of the buried phenyl ring with an active site tryptophan residue and hydrogen bonding between the carboxyl group of the inhibitor and the catalytically active residues Y48 and H110 (*26*). Furthermore, a recent crystal structure of IDD743 in the active site of *h*ALR2 has confirmed that the original model structure replicated the actual position of the inhibitor reliably (*17*, *33*). Because the identical structural components are also present on **1**, the high reproducibility of this binding motif gives us confidence that modeling the inhibitor **1** into the active site this way is a reasonable estimate of the actual structure of this system until a complete crystal structure is available. Furthermore, extensive molecular dynamics simulations of this system are underway and will be reported in a later publication. As demonstrated below, small variations in the structure that would likely not be distinguishable by X-ray crystallography or that could change easily with temperature (most high-resolution structures are solved at low temperature) or cryoprotectant, can produce very large *local* changes in the electrostatic field which can be detected by VSE spectroscopy.

Modeling the nitrile bond onto the IDD-type structures seen in the high-resolution crystal structure gave a distance between the N atom of the nitrile and the O of a nearby residue T113 of <2 Å. Given this unrealistic distance, in the model structure T113 was rotated around the $C_\alpha-C_\beta$ bond to move the oxygen away from the nitrile. Although protein crystallography studies are ongoing to determine the actual structure of the *h*ALR2/**1**/$NADP^+$ system, in the absence of these structures this is a reasonable compromise to model the inhibitor into this protein.

(1) Mutations Predicted To Cause a Large Change in Electrostatic Field. The first strategy used to identify *h*ALR2 mutants to express and study was based on computational predictions of perturbations that would cause a large change in protein field. Previous work in our laboratory has relied on a Poisson−Boltzmann equation (PBE) continuum electrostatics technique to predict changes in electrostatic field caused by amino acid mutations. A significant drawback of continuum electrostatics calculations for investigating local electrostatic fields over the distance of a few amino acids is that it is extremely sensitive to small changes in the structure that is input into the calculation (*17*). The model structure

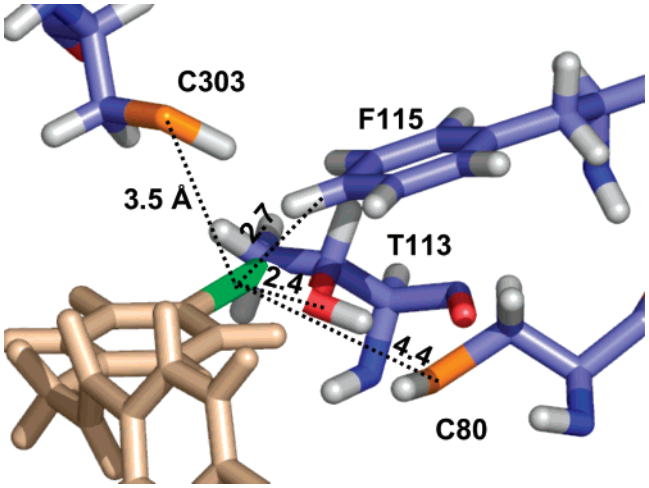

FIGURE 3: Expanded view of the phenyl ring of **1** bearing the nitrile functional group (green) bound to WT *h*ALR2 showing nearby amino acid residues that were selected for mutagenesis, C80, T113, F115, and C303. Distances from residues to the carbon atom of the C≡N bond are noted in angstroms. The model is adapted from the crystal structures of similar molecules in *h*ALR2 (*31*, *32*).

of **1** in *h*ALR2 is still only an approximation derived from crystal structures of slightly different inhibitors in the WT protein. While this strategy has recently been validated with a crystal structure of a previous inhibitor, IDD743 (*33*), it is important to remember this caveat. X-ray studies of **1** in *h*ALR2 are in progress.

A continuum electrostatics calculation screen was run to identify mutations in the vicinity of the inhibitor's nitrile group that would cause large perturbations in the protein's electrostatic field. Five mutations at positions shown in Figure 3 were selected for protein expression and spectroscopy. The largely hydrophobic active site has one threonine residue, T113, which lies quite near the inhibitor's nitrile bond and appeared as an ideal candidate to remove a polar group from the active site. This was mutated to both alanine and valine to study the convolution of electrostatic and steric perturbations on the probe. A second residue, F115, located ~3 Å above the plane of the nitrile bond axis, was mutated to tyrosine to introduce a polar functional group with minimal structural perturbation. Cysteine 303 was mutated to asparagine to introduce polar groups in place of the hydrophobic cysteine residue. Finally, cysteine 80 was mutated to alanine, which was predicted by DelPhi not to cause a major perturbation in the protein electrostatic field.

Typical FTIR spectra of the nitrile group of **1** bound to WT, T113A, and F115Y are shown in Figure 4, and values of $\Delta\bar{\nu}_{obs}$ and $\Delta\vec{F}_{protein}$ for all mutants examined are given in Table 1. The large shifts in absorption energy of the inhibitor nitrile functional group ($\Delta\bar{\nu}_{obs}$= −6.6 cm^{-1} for T113A and −4.5 cm^{-1} for F115Y vs WT) were clearly resolved by our instrument (0.5 cm^{-1} resolution). Given the value of $\Delta\vec{\mu}_{CN}$ of 0.77 cm^{-1}/(MV/cm), these energy shifts correspond to changes in the protein electrostatic field, $\Delta\vec{F}_{protein}$, of −8.6 and −5.7 MV/cm for the mutations T113A and F115Y, respectively (eq 3). The mutations T113V and C303N, which respectively remove and add polarity, also caused large $\Delta\vec{F}_{protein}$ of −4.5 (T113V) and −3.2 MV/cm (C303N). Finally, the mutant C80A, which was predicted not to perturb the protein's electrostatic field significantly, did result in a much smaller but measurable $\Delta\vec{F}_{protein}$ = −1.0 MV/cm.

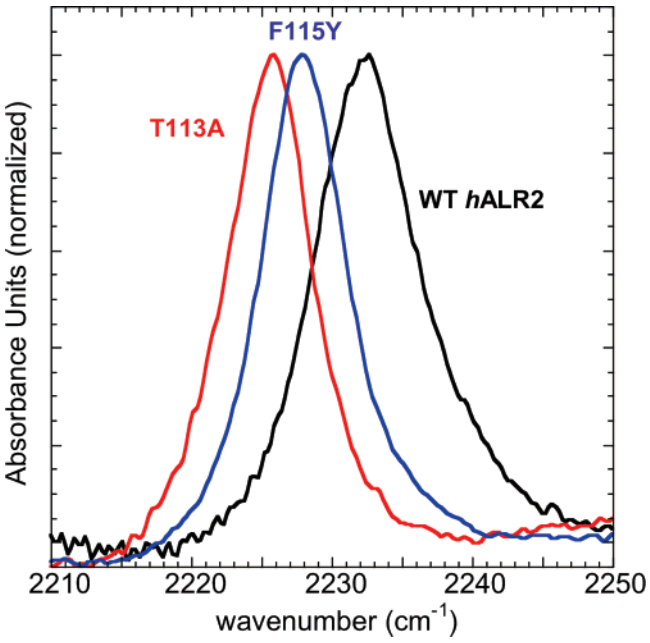

FIGURE 4: Vibrational absorption spectra in the nitrile region of **1** bound to WT *h*ALR2 (black, $\Delta\bar{\nu}_{obs}$= 2232.5 cm^{-1}), and mutants F115Y (blue, $\Delta\bar{\nu}_{obs}$= 2228.0 cm^{-1}) and T113A (red, 2225.8 cm^{-1}).

The continuum electrostatics calculations that were preformed to predict mutations that would cause large $\Delta\vec{F}_{protein}$ were found to be inaccurate in these cases. The mutant T113A, for example, was predicted to cause a change in the protein field of +2.1 MV/cm, but was measured to change the field by −8.6 MV/cm. Continuum electrostatics provided very poor predictions of electrostatic fields, even in this ideal protein/inhibitor system. In some cases, these large differences may be due to the sensitivity of the calculation to local details of the protein structure (*47*). For example, in the case of the mutation F115Y there are two physically reasonable orientations for the hydroxyl group of the tyrosine to assume, which are shown side-by-side in Figure 5. The direction of the hydroxyl hydrogen on the mutated side chain causes a radically different prediction of $\Delta\vec{F}_{protein}$: either −12.4 or +7.1 MV/cm. Both IR and activity measurements are measured at room temperature, and it is likely that neither extreme conformation will prevail and the OH bond will rotate to some degree around the phenyl C−O bond. Interestingly, there is no evidence from the line shape for underlying structure or inhomogeneous broadening that is different from what is observed in other mutants. High quality X-ray structures of the sort previously published for *h*ALR2/**1**/NADP$^+$ complexes include information on side-chain conformational disorder, though these ultrahigh resolution structures are carried out at low temperature. Molecular dynamics simulations of the structure run at room temperature can supply conformational statistics of the range of motion of those side chains under the ambient conditions of the VSE spectroscopy experiment. These highly local effects will not influence the overall electrostatic calculation across the entire protein, but will matter tremendously for specific ligand binding and catalysis. Previous work in our laboratory on a C≡N bond placed in *h*ALR2 found that continuum electrostatics calculations could be improved significantly with molecular dynamics (MD) simulations (*17*), and this work is underway on the *h*ALR2/**1**/NADP$^+$ system. Because of the lack of a crystal structure of the *h*ALR2/**1**/NADP$^+$ complex, no electrostatics calculations on double mutant structures such as T113A/C303N were attempted.

(2) Removal of a Possible Hydrogen Bond to the Nitrile Group. The concept of interpreting Stark shifts as a measure of electrostatic fields requires that the Stark tuning rate $\Delta\vec{\mu}_{CN}$ should be constant, independent of the environment, and insensitive to local bonding interactions. The best way to test this is to perform the vibrational Stark measurements on the probe in the protein as was done with CO and NO bound to myoglobin mutants (*34*, *35*). This was possible because the Stark tuning rate for CO and NO bound to the heme iron is very large. The corresponding experiment would be difficult with the *h*ALR2/**1**/NADP$^+$ complex because of the relatively smaller Stark tuning rate and absorptivity of the nitrile. Previous theoretical analysis of vibrational spectroscopy of acetonitrile dissolved in alcohol solvents has shown that, when the C≡N group's nitrogen atom acts as a hydrogen bond acceptor, the absorption energy of the C≡N bond is perturbed independently of electrostatic effects (*48*). The proximity of the C≡N bond of inhibitor **1** to the hydroxyl group of T113 (modeled at <2 Å for the N···O distance, Figure 3) is therefore a possible complication for measuring electrostatic fields in this region of *h*ALR2 with a nitrile probe. Because the estimate of the location of the C≡N is from a model of **1** in a crystal structure solved with a different inhibitor, it is possible that in the *h*ALR2/**1**/NADP$^+$ complex the nitrile bond will not be so close to the T113 hydroxyl group, and X-ray studies of **1** in WT and mutant *h*ALR2 are in progress. Until crystal structures are available to refine the structural model, this question was investigated empirically with three mutants, T113A/C303N, T113A/C303D, and T113A/S302R/C303D, to compare the effect of the T113 side chain on the measured electrostatic field. By comparing the electrostatic effects of the mutations C303N, C303D, and S302R/C303D relative to WT *h*ALR2 versus T113A, it was possible to investigate whether T113 was influencing the vibrational Stark effect in a manner not described by eq 3.

The single mutant C303D had $\Delta\vec{F}_{protein}$ of −6.5 MV/cm, approximately twice that of the mutant C303N ($\Delta\vec{F}_{protein}$ = −3.2 MV/cm, Table 1). When T113 was converted to alanine in the double mutants, this trend was reversed, with T113A/C303N displaying the larger $\Delta\vec{F}_{protein}$ (−10.4 MV/cm vs −7.3 MV/cm for T113A/C303D). When compared to the WT protein, both mutations C303D and C303N shifted the nitrile's absorption maximum to lower energy, or negative $\Delta\vec{F}_{protein}$. When compared to T113A, however, while the double mutant T113A/C303N still shifted the nitrile's absorption maximum to lower energy (2224.5 cm^{-1} for T113A/C303N vs 2225.8 cm^{-1} for T113A), the opposite was seen for the double mutant T113A/C303D, which was found to have a nitrile peak at 2226.8 cm^{-1}, higher than that of T113A. The difference between T113A and T113A/S302R/C303D ($\bar{\nu}_{obs}$= 2231.8 cm^{-1}) was even more dramatic. This means that although both of the mutations C303D and S302R/C303D caused a negative $\Delta\vec{F}_{protein}$ when compared to WT, they caused a positive $\Delta\vec{F}_{protein}$ when compared to T113A. While hydrogen bonding to the C≡N probe could possibly affect the magnitude of the Stark tuning rate, it is very unlikely that it would alter the direction of the bond dipole, which would have to be the case if this observation

Table 1: Measured Inhibition Constants and Vibrational Frequencies of Inhibitor **1** in the Active Site of WT and Mutant *h*ALR2. $\Delta\bar{\nu}_{obs}$, $\Delta\vec{F}_{protein}$, and $\Delta\vec{F}_{predicted}$ Predicted of Each Mutant vs WT[a]

mutation	K_I' (nM)	$\bar{\nu}_{obs}$ (cm^{-1})	$\Delta\bar{\nu}_{obs}$ (cm^{-1})	$\Delta\vec{F}_{protein}$ (MV/cm)	$\Delta\vec{F}_{predicted}$ (MV/cm)
WT	2000 ± 600	2232.5 ± 0.4			
		Mutations That Introduce or Remove Polar or Charged Residues			
T113A	110 ± 70	2225.8 ± 0.2	−6.6	−8.6	+2.1
F115Y	620 ± 30	2228.0 ± 0.1	−4.5	−5.7	−12.4, +7.1[b]
T113V	290 ± 90	2229.0 ± 0.2	−3.5	−4.5	+2.3
C303N	800 ± 40	2229.9 ± 0.4	−2.5	−3.2	−2.9, +8.7[b]
C80A	4600	2231.7 ± 0.1	−0.8	−1.0	−0.5
		Mutations That Remove H-Bonding			
T113A/C303N	60 ± 40	2224.5 ± 0.1	−8.0	−10.4	*c*
T113A/C303D	40	2226.8 ± 0.1	−5.6	−7.3	*c*
T113A/S302R/C303D		2231.8 ± 0.7	−0.7	−0.9	*c*
		Mutations That Revert *h*ALR2 to *h*ALR1			
C80N	2000	2232.7 ± 0.1	+0.2	0.3	−2.4, +2.3[b]
T113Y	3900 ± 500	2231.7 ± 0.1	−0.8	−1.0	*d*
C303D	510 ± 100	2227.5 ± 0.1	−5.0	−6.5	−3.7, +18.4[b]
S302R/C303D	290 ± 90	2228.9 ± 0.1	−3.6	−4.7	*c*
T113Y/S302R/C303D	4000 ± 3000	2229.4 ± 0.5	−3.1	−4.0	*c*
C80N/T113Y/S302R/C303D	7800	2227.1 ± 0.3	−5.4	−7.0	*c*

[a] Errors reported for K_I' and $\Delta\bar{\nu}_{obs}$ are one standard deviation of multiple experiments. [b] Range of estimates of $\Delta\vec{F}_{predicted}$ were calculated from at least two reasonable orientations of the mutated side chain residue. The reported numbers are the low and high estimate of $\Delta\vec{F}_{predicted}$. [c] Continuum electrostatic calculations were not run because of the large number of possible conformations of multiple amino acid mutations. [d] Continuum electrostatic calculations were not run because of uncertainty about the position of **1** in the active site of *h*ALR2 with the large steric perturbation caused by the T113Y mutation.

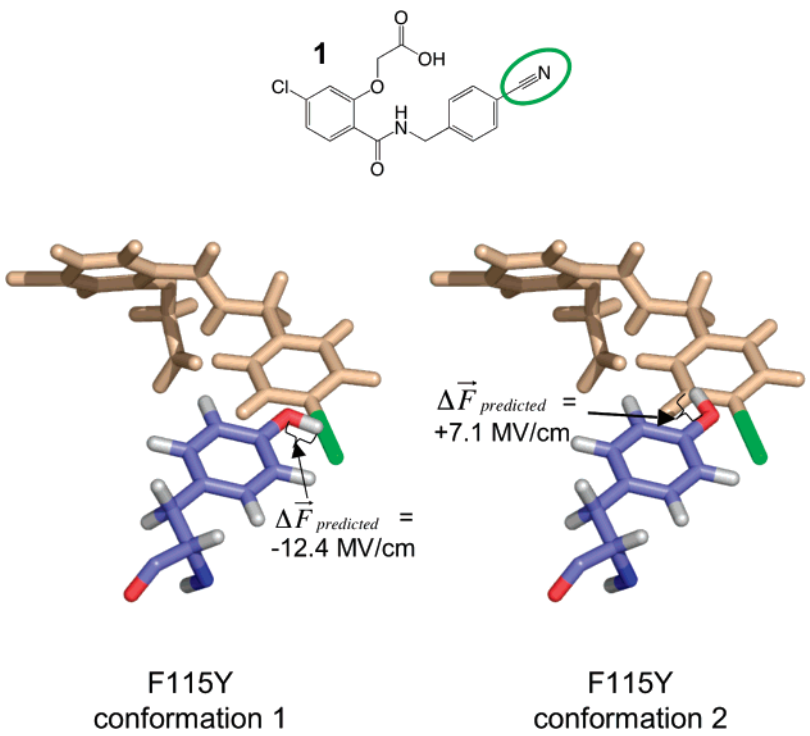

FIGURE 5: Two possible orientations of the mutation F115Y relative to inhibitor **1** and the corresponding $\Delta\vec{F}_{predicted}$. The only difference between the two structures is the orientation of the hydroxyl hydrogen atom of the side chain, which leads to a $\Delta F_{predicted}$ of either −12.4 or +7.1 MV/cm.

were due purely to significant change in the Stark tuning rate caused by hydrogen bonding to the nitrile.

Interestingly, the double mutant T113A/F115Y had the smallest k_{cat} of any mutant surveyed in this study (0.30 ± 0.06 s^{-1} for WT *h*ALR2 vs ∼0.03 s^{-1} for T113A/F115Y) even though the single mutants T113A and F115Y were both stable and active. Furthermore, T113A/F115Y was also the only mutant of *h*ALR2 expressed in this study that did not bind to inhibitor **1** with sufficiently high K_I' for IR experiments. This may indicate that the active site of the T113A/X mutants is sufficiently perturbed from the WT enzyme that it is not reasonable to compare changes in the protein field through this strategy.

(3) Comparison to Structurally Similar Proteins. The third strategy for selecting mutations was inspired by examination of a protein that is structurally similar to *h*ALR2, human aldehyde reductase (*h*ALR1). These two proteins have >85% sequence homology, and most importantly, the structures of

their active sites are almost identical (*29*). The similarity between these two proteins has frustrated attempts to design inhibitor drugs for the treatment of diabetes that bind exclusively to *h*ALR2 without affecting *h*ALR1 (*29*). Direct measurements of electrostatic fields in these two enzymes would be an important contribution to elucidating the reasons for this, particularly because traditional structural-based approaches to drug design have not proven fruitful.

In an effort to examine the effect of electrostatic field on two structurally similar proteins, *h*ALR2 and *h*ALR1, five mutations were made that revert the active site of *h*ALR2 to what are found at the same locations in *h*ALR1. Seven active site residues differ between the two enzymes (30% of the total number of residues lining the active site); four of these differences are within 8 Å of the nitrile bond of inhibitor **1**: C80/N82 (*h*ALR2/*h*ALR1), T113/Y115, S302R/R311, and C303/D312. Therefore the mutations T113Y, C80N, S302R, and C303D were made to *h*ALR2 in various combinations to determine how these changes, which cause virtually no structural perturbation, might influence the active site electrostatic field. The mutation C303D made by far the largest effect on the electrostatic field of the active site, shifting it by −6.5 MV/cm. When the additional mutations S302R and T113Y were added to the background of this mutation, $\Delta\vec{F}_{\text{protein}}$ was reduced somewhat, but this was reversed when the final reversion mutation, C80N/T113Y/S302R/C303D, demonstrated one of the largest active site perturbations observed in this study ($\Delta\vec{F}_{\text{protein}} = -7.0$ MV/cm).

Considering all the mutations studied as a group, several trends were observed. Examination of Table 1 shows that with the exception of the mutant C80N, which caused the absorption energy of the nitrile bond to shift by a small amount (0.2 cm^{-1}) higher in energy, all the mutations studied here caused large shifts to lower energy. This indicates that all mutations studied here caused a lower absolute value of the protein field. This was the case for both adding (F115Y, C303N) and removing (T113A/V) polar groups from the active site. The largest electrostatic field perturbation measured with this system was in the double mutant T113A/C303N, which shifted the absorption energy of the nitrile group lower in energy by 8 cm^{-1}, corresponding to $\Delta\vec{F}_{\text{protein}}$ of −10.4 MV/cm. A similar study on *aldehyde* reductase is currently underway.

(4) Correlations between Electrostatic Fields and Enzyme Inhibition. It has long been speculated that the role of an enzyme's active site is preorganization of the electrostatic configuration of the transition state, not necessarily in structural or dynamic organization (*9, 49*). This study uses a nonnatural substrate (nitrile group on an inhibitor) to probe a region of *h*ALR2's active site that is far removed from the catalytically important residues Y48 and H110 (*20, 26, 27*), so it is not testing this electrostatic hypothesis directly. Furthermore, detailed computational studies of the electrostatic effects on *h*ALR2 catalysis concluded that they are relatively small in this active site (*20, 27*). Directly measuring electrostatic field changes caused by a wide variety of amino acid mutations, all of which perturb the active site in the same way, i.e., $\Delta\vec{F}_{\text{protein}} < 0$ MV/cm, raises the interesting possibility that this active site is indeed organized to support a particular electrostatic interaction between the enzyme and its substrate. An example of the biological importance of

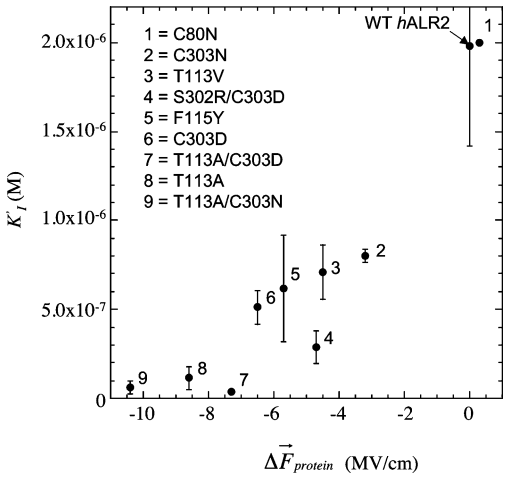

FIGURE 6: Inhibition constant of **1** (K'_I) shown vs measured $\Delta\vec{F}_{\text{protein}}$ of **1** for WT *h*ALR2 (indicated on plot) and several mutants. Values for K'_I are given in Table 1, and error bars are one standard deviation in K'_I measured on at least two repeats of protein expression and purification. 1 = C80N; 2 = C303N; 3 = T113V; 4 = S302R/C303D; 5 = F115Y; 6 = C303D; 7 = T113A/C303D; 8 = T113A; 9 = T113A/C303N. Four mutants given in Table 1 (C80A, T113Y, T113Y/S302R/C303D, and C80N/T113Y/S302R/C303D) are not shown on the plot.

electrostatic field can be seen clearly in the kinetics of inhibition of *h*ALR2 with **1**, shown in Figure 6. There is a clear trend between the measured strength of the electrostatic field of each mutant compared to WT *h*ALR2, $\Delta\vec{F}_{\text{protein}}$, and the measured inhibition constant, K'_I, of **1** in that mutant. As $\Delta\vec{F}_{\text{protein}}$, measured at the midpoint of the nitrile bond, decreased, the inhibition constant of inhibitor **1** to *h*ALR2 activity, K'_I, decreased in value, i.e., became a more potent *h*ALR2 inhibitor. This could be due to electrostatic field stabilization of the nitrile bond ground state dipole, $\vec{\mu}_{\text{CN}}$, which points in the same direction as the difference dipole, $\Delta\vec{\mu}_{\text{CN}}$ (*44*). This is evidence that a thorough understanding of electrostatic differences between the active sites of *h*ALR2 and *h*ALR1 might enable the design of more efficient inhibitors of *h*ALR2. Interestingly, all three mutants containing the T113Y mutation did not display K'_I that followed the trend seen in Figure 6, but instead had dramatically higher K'_I ($> 4 \times 10^{-6}$ M) than WT *h*ALR2, even though all of these mutations also had $\Delta\vec{F}_{\text{protein}} < 0$ (Table 1). This could be due to the significant size perturbation of the T113Y mutation, or could relate to important electrostatic differences between the active sites of *h*ALR2 and *h*ALR1. We are currently performing the identical experiment on *h*ALR1 to determine if these particular mutations are responsible for electrostatic differences between these two enzymes that could explain differences in their mechanism or reactivity. These experiments offer the promise of directly measuring electrostatic influences on an enzyme that would be missed by a straightforward structure−function analysis.

CONCLUSION

This work demonstrates that when the nitrile Stark vibrational probe is removed from water and placed in a buried region of a protein, nitrile infrared absorption energy shifts based on electrostatic perturbations are unambiguous, easy to measure, and provide a facile, direct way to quantify electrostatic fields in the vicinity of the protein. The magnitude of $\Delta\vec{F}_{\text{protein}}$ observed in these studies, > -10 MV/

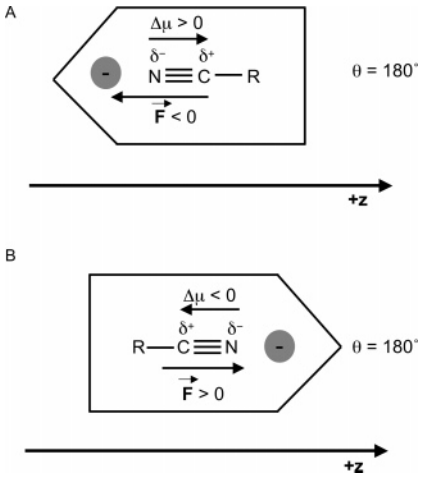

FIGURE 7: Schematic representation of two possible coordinate axes to define the direction of $\Delta\vec{\mu}_{CN}$. In both cases the nitrile bond is in an asymmetrical box representing a protein where the dominate electrostatic field is caused by a cloud of negative charge near the nitrogen atom of the nitrile. (A) The difference dipole $\Delta\vec{\mu}_{CN} > 0$; (B) $\Delta\vec{\mu}_{CN} < 0$.

cm, is similar to what has been seen before only with the more limited metal-bound CO and NO VSE probes. Because the nitrile probe can be either covalently bonded to the protein itself or introduced on a tight-binding ligand, it has potentially many more applications than CO or NO. This work demonstrates that VSE spectroscopy with the nitrile probe can be extended to many protein systems of interest as a general tool for measuring electrostatic fields in proteins.

APPENDIX

The difference dipole of the nitrile bond, $\Delta\vec{\mu}_{CN}$, which relates the measured $\Delta\nu_{obs}hc = \Delta E$ and $\Delta\vec{F}_{protein}$, has been shown for nitrile probes to point from the nitrogen atom to the carbon atom parallel to the internuclear bond axis (*44*). It is therefore possible to use VSE spectroscopy to measure the direction of the local electrostatic field along a probe vibration as well as its magnitude, and because of this it is important to define clearly the coordinate system used in this work. This is necessary for two reasons. First, VSE spectroscopy has thus far been used to measure only a single probe inserted into a protein, but future studies may use two independent and spectroscopically resolvable vibrational Stark probes. In this situation it will be necessary to define clearly the angle of $\Delta\vec{\mu}$ of both probes with respect to the coordinate axis. Second, measured values of $\Delta\vec{F}_{protein}$ are being compared in this study directly to calculated predictions, $\Delta\vec{F}_{predicted}$, using a Poisson−Boltzmann equation continuum electrostatics-based approach, which requires a coordinate system to be imposed on the protein. The direction of this coordinate system with respect to $\Delta\vec{\mu}_{CN}$ will alter interpretations of the direction of both $\Delta\vec{F}_{protein}$ and $\Delta\vec{F}_{predicted}$. Choice of the coordinate axis is arbitrary, although once chosen it must be clearly defined and remain fixed. We continue our development of VSE spectroscopy by briefly describing the choice of coordinate axis system here.

For convenience, any coordinate system will have its origin be at the midpoint of the C≡N bond, with the *z*-axis parallel to the nitrile bond and intersecting both the carbon and nitrogen atoms. Two possible orientations of the *z*-axis are shown in Figure 7, in which the R−C≡N group has been placed in an asymmetric box representing a protein environment, and where the dominate electrostatic field at the nitrile bond is caused by a cloud of negative charge near the nitrogen atom. Although VSE spectroscopy can only measure changes in protein electrostatic field upon making some perturbation, this discussion will be simplified by considering only the direction of this hypothetical field, $\vec{F}$, caused by the cloud of negative charge. In Figure 7A, the positive *z*-axis points from the nitrogen to the carbon, parallel to the difference dipole $\Delta\vec{\mu}_{CN}$. This corresponds to the standard definition of the direction of a dipole, and $\Delta\vec{\mu}_{CN} > 0$. The electrostatic field along the axis of the nitrile, $\vec{F}$, whose direction is defined by the direction in which a positive test charge dropped into that field would move, therefore points toward the minus *z*-axis and is less than zero (i.e., increasing in the minus *z* direction). In this scenario, $\Delta\vec{\mu}_{CN}$ and $\vec{F}$ point in opposite directions, and the angle, θ, separating them is 180°. The energy of this interaction is

$$\Delta E = -\Delta\vec{\mu}_{CN}\cdot\vec{F} = -|\Delta\vec{\mu}_{CN}||\vec{F}|\cos\theta \qquad (4)$$

and $\Delta E > 0$. In this scenario, ΔE scales as the negative of $\vec{F}$: i.e., ΔE decreases as $\vec{F}$ increases.

The opposite scenario is shown in Figure 7B, where the protein has been rotated so that the positive *z*-axis points from the carbon to the nitrogen of the nitrile, but the electrostatic environment of the nitrile bond itself in the protein remains identical to the situation in Figure 7A. In this scenario, $\Delta\vec{\mu}_{CN} < 0$, while $\vec{F} > 0$ because the field is increasing in the direction of the plus *z*-axis. The angle θ between these two vectors remains 180° and $\Delta E > 0$, the same result found from the scenario shown in Figure 7A. This is physically appropriate because the nature of the nitrile in the protein does not change when the arbitrary bond axis imposed by the experiment changes. In this scenario, ΔE scales as positive $\vec{F}$ (i.e., as $\vec{F}$ increases, ΔE increases also) but only with respect to the direction of the coordinate axis. In both Figures 7A and B, the field points toward the nitrogen atom of the nitrile.

Previous work on VSE spectroscopy has used the coordinate system shown in Figure 7B, with the positive *z*-axis pointing from the carbon to the nitrogen of the nitrile, and $\Delta\vec{\mu}_{CN} < 0$. In this case, an amino acid mutation that causes a change in electrostatic field of +1.0 MV/cm along the nitrile will cause a shift in nitrile stretching frequency of $+|\Delta\vec{\mu}_{CN}|$ cm^{-1}. Maintaining this axis definition here is consistent with previous literature in which the theoretical and experimental development of VSE spectroscopy is explained in detail. Defining $\Delta\vec{\mu}_{CN} < 0$ is equivalent to fixing the angle between $|\Delta\vec{\mu}_{CN}|$ and the coordinate axis as 180°, and thus an observed shift in the absorbance frequency of the nitrile probe of 0.77 cm^{-1} corresponds to an increase in electrostatic field of 1.0 MV/cm in the direction of the nitrogen atom of the nitrile. Preliminary work in this laboratory has shown the advantage of using two independent and resolvable vibrational Stark probes in a single protein, and this is predicted to become an important application of VSE spectroscopy (*50*). In this situation it will be necessary to define clearly the angle of $\Delta\vec{\mu}$ of both probes with respect to the coordinate axis, where at least one of those angles will be something other than 0° or 180°.

ACKNOWLEDGMENT

We thank D. L. Ensign for computing charges and radii for **1** and $NADP^+$ and I. T. Suydam for compiling the *h*ALR2/**1**/$NADP^+$ model structure.

REFERENCES

1. Honig, B., and Nicholls, A. (1995) Classical Electrostatics in Biology and Chemistry, *Science 268*, 1144−1149.
2. Warshel, A., and Papazyan, A. (1998) Electrostatic effects in macromolecules: fundamental concepts and practical modeling, *Curr. Opin. Struct. Biol. 8*, 211−217.
3. Simonson, T. (2001) Macromolecular electrostatics: continuum models and their growing pains, *Curr. Opin. Struct. Biol. 11*, 243−252.
4. Nielsen, J. E., Andersen, K. V., Honig, B., Hooft, R. W. W., Klebe, G., Vriend, G., and Wade, R. C. (1999) Improving Macromolecular Electrostatics Calculations, *Protein Eng. 12*, 657−662.
5. Gunner, M. R., Nicholls, A., and Honig, B. (1996) Electrostatic Potentials in Rhodopseudomonas viridis Reaction Centers: Implications for the Driving Force and Directionality of Electron Transfer, *J. Phys. Chem. 100*, 4277−4291.
6. Lockhart, D. J., Kirmaier, C., Holten, D., and Boxer, S. G. (1990) Electric Field Effects on the Initial Electron-Transfer Kinetcis in Bacterial Photosynthetic Reaction Centers, *J. Phys. Chem. 94*, 6987−6995.
7. Villa, J., and Warshel, A. (2001) Energetics and Dynamics of Enzymatic Reactions, *J. Phys. Chem. B 105*, 7887−7907.
8. Lee, L. P., and Tidor, B. (2001) Optimization of Binding Electrostatics: Charge Complementarity in the Barnase-Barstar Protein Complex, *Protein Sci. 10*, 362−377.
9. Warshel, A., Sharma, P. K., Kato, M., and Parson, W. W. (2006) Modeling electrostatic effects in proteins, *Biochim. Biophys. Acta 1764*, 1647−1676.
10. Forsyth, W. R., Antosiewicz, J. M., and Robertson, A. D. (2002) Empirical Relationships Between Protein Structure and Carboxyl pKa values in Proteins, *Proteins 48*, 388−403.
11. Schutz, C. N., and Warshel, A. (2001) What are Dielectric "Constants" of Proteins and How to Validate Electrostatic Models, *Proteins 44*, 400−417.
12. MacDermaid, C. M., and Kaminski, G. A. (2007) Electrostatic Polarization is Crucial for Reproducing pKa Shifts of Carboxylic Residues in Turkey Ovomucoid Third Domain, *J. Phys. Chem. B 111*, 9036−9044.
13. Khandogin, J., and Brooks, C. L. (2006) Toward the Accurate First-Principles Prediction of Ionization Equilibria in Proteins, *Biochemistry 45*, 9363−9373.
14. Danielson, M. A., and Falke, J. J. (1996) Use of 19FNMR To Probe Protein Structure and Conformational Changes, *Annu. Rev. Biophys. Biomol. Struct. 25*, 163−195.
15. Pearson, J. G., Oldfield, E., Lee, F. S., and Warshel, A. (1993) Chemical Shifts in Proteins: A Shielding Trajectory Analysis of the Fluorine Nuclear Magnetic Resonance Spectrum of the Escherichia coli Galactose Binding Protein Using a Multipole Shielding Polarizability-Local Reaction Field-Molecular Dynamics Approach, *J. Am. Chem. Soc. 115*, 6851−6862.
16. Schubert, M., Poon, D. K. Y., Wicki, J., Tarling, C. A., Kwan, E. M., Nielsen, J. E., Withers, S. G., and McIntosh, L. P. (2007) Probing Electrostatic Interactions along the Reaction Pathway of a Glycoside Hydrolase: Histidine Characterization by NMR Spectroscopy, *Biochemistry 46*, 7383−7395.
17. Suydam, I. T., Snow, C. D., Pande, V. S., and Boxer, S. G. (2006) Electric Fields at the Active Site of an Enzyme: Direct Comparison of Experiment with Theory, *Science 313*, 200−204.
18. Park, E. S., Andrews, S. S., Hu, R. B., and Boxer, S. G. (1999) Vibrational Stark Spectroscopy in Proteins: A Probe and Calibration for Electrostatic Fields, *J. Phys. Chem. B 103*, 9813−9817.
19. Suydam, I. T., and Boxer, S. G. (2003) Vibrational Stark Effects Calibrate the Sensitivity of Vibrational Probes for Electric Fields in Proteins, *Biochemistry 42*, 12050−12055.
20. Varnai, P., and Warshel, A. (2000) Computer Simulation Studies of the Catalytic Mechanism of Human Aldose Reductase, *J. Am. Chem. Soc. 122*, 3849−3860.
21. Bohren, K. M., Page, J. L., Shankar, R., Henry, S. P., and Gabbay, K. H. (1991) Expression of Human Aldose and Aldehyde Reductases, *J. Biol. Chem. 266*, 24031−24037.
22. Kaul, C. L., and Ramarao, P. (2001) The Role of Aldose Reductase Inhibitors in Diabetic Complications: Recent Trends, *Methods Find. Exp. Clin. Pharmacol. 23*, 465−475.
23. Vander Jagt, D. L., Kolb, N. S., Vander Jagt, T. J., Chino, J., Martinez, F. J., Hunsaker, L. A., and Royer, R. E. (1995) Substrate specificity of human aldose reductase: indentification of 4-hydroxynonenal as an endogenous substrate, *Biochim. Biophys. Acta 1249*, 117−126.
24. Obrosova, I. G., Faller, A., Burgan, J., Ostrow, E., and Williamson, J. R. (1997) Glycolytic pathyway, redox state of NAD(P)-couples and energy metabolism in lens in galactose-fed rats: effect of an aldose reductase inhibitor, *Curr. Eye Res. 16*, 34−43.
25. Kador, P. F. (1988) The Role of Aldose Reductase in the Development of Diabetic Complications, *Med. Res. Rev. 8*, 325−352.
26. Bohren, K. M., Grimshaw, C. E., Lai, C. J., Harrison, D. H., Ringe, D., Petsko, G. A., and Gabbay, K. H. (1994) Tyrosine-48 Is the Proton Donor and Histidine-110 Directs Substrate Stereochemical Selectivity in the Reduction Reaction of Human Aldose Reductase: Enzyme Kinetics and Crystal Structure of the Y48H Mutant Enzyme, *Biochemistry 33*, 2021−2032.
27. Varnai, P., Richards, W. G., and Lyne, P. D. (1999) Modelling the Catalytic Reaction in Human Aldose Reductase, *Proteins 37*, 218−227.
28. Obrosova, I. G., and Fatallah, L. (2000) Evaluation of an aldose reductase inhibitor on lens metabolism, ATPases and antioxidative defensein streptozotocin-diabetic rats: an intervention study, *Diabetologia 43*, 1048−1055.
29. Van Zandt, M. C., Sibley, E. O., McCann, E. E., Combs, K. J., Flam, B., Sawicki, D. R., Sabetta, A., Carrington, A., Sredy, J., Howard, E., Mitschler, A., and Podjarny, A. (2004) Design and synthesis of highly potent and selective (2-arylcarbamoyl-phenoxy)-acetic acid inhibitors of aldose reductase for treatment of chronic diabetic complications, *Bioorgan. Med. Chem. 12*, 5661−5675.
30. Steuber, H., Zentgraf, M., Podjarny, A., Heine, A., and Klebe, G. (2006) High-resolution Crystal Structure of Aldose Reductase Complexed with the Novel Sulfonyl-pyridazinone Inhibitor Exhibiting an Alternative Active Site Anchoring Group, *J. Mol. Biol. 356*, 45−56.
31. Podjarny, A., Cachau, R. E., Schneider, T., Van Zandt, M. C., and Joachimiak, A. (2004) Subatomic and atomic crystallographic studies of aldose reductase: implications for inhibitor binding, *Cell. Mol. Life Sci. 61*, 763−773.
32. Howard, E. I., Sanishvili, R., Cachau, R. E., Mitschler, A., Chevrier, B., Barth, P., Lamour, V., Van Zandt, M. C., Sibley, E. O., Bon, C., Moras, D., Schneider, T. R., Joachimiak, A., and Podjarny, A. (2004) Ultrahigh Resolution Drug Design I: Details of Interactions in Human Aldose Reductase-Inhibitor Complex at 0.66 A, *Proteins 55*, 792−804.
33. Podjarny, A. Personal communication.
34. Park, E. S., and Boxer, S. G. (2002) Origins of the Sensitivity of Molecular Vibrations to Electric Fields: Carboyl and Nitrosyl Stretches in Model Compounds and Proteins, *J. Phys. Chem. B 106*, 5800−5806.
35. Park, E. S., Thomas, M. R., and Boxer, S. G. (2000) Vibrational Stark Spectroscopy of NO Bound to Heme: Effects of Protein Electrostatic Fields on the NO Stretch Frequency, *J. Am. Chem. Soc. 122*, 12297−12303.
36. Lamour, V., Barth, P., Rogniaux, H., Poterszman, A., Howard, E., Mitschler, A., Van Dorsselaer, A., Podjarny, A., and Motas, D. (1999) Production of crystals of human aldose reductase with very high resolution diffraction, *Acta Cystallogr. 55*, 721−723.
37. Kurono, M., Fujiwara, I., and Yoshida, K. (2001) Stereospecific interaction of a novel spirosuccinimide type aldose reductase inhibitor, AS-3201, with aldose reductase, *Biochemistry 40*, 8216−8226.
38. DeLano, W. L. www.pymol.sourceforge.net.
39. Rocchia, W., Alexov, E., and Honig, B. (2001) Extending the applicability of the nonlinear Poisson-Boltzmann equation: Multiple dielectric constatns and multivalent ions, *J. Phys. Chem. B 105*, 6507−6514.
40. Sharp, K., and Honig, B. (1989) Lattice Models of Electrostatic Interactions - The Finite- Difference Poisson-Boltzmann Method, *Chem. Scr. 29A*, 71−74.
41. Sitkoff, D., Sharp, K., and Honig, B. (1994) Accurate Calculation of Hydration Free Energies Using Macroscopic Solvent Models, *J. Phys. Chem. 98*, 1978−1988.

42. amber.scripps.edu/antechamber/ac.html.
43. Andrews, S. S., and Boxer, S. G. (2000) Vibrational Stark Effects of Nitriles I. Methods and Experimental Results, *J. Phys. Chem. A 104*, 11853−11863.
44. Andrews, S. S., and Boxer, S. G. (2002) Vibrational Stark Effects of Nitriles II. Physical Origins of Stark Effects from Experiment and Perturbation Models, *J. Phys. Chem. A 106*, 469−477.
45. Suydam, I. T. The Measurement and Prediction of Electric Fields in the Active Site of Human Aldose Reductase, Stanford University 2005.
46. Steuber, H., Heine, A., and Klebe, G. (2007) Structural and thermodynamic study on aldose reductase: nitro-substiuted inhibitors with strong enthalpic binding contribution, *J. Mol. Biol. 368*, 618−638.
47. Parson, W. W., Chu, Z. T., and Warshel, A. (1990) Electrostatic control of charge separation in bacterial photosynthesis, *Biochim. Biophys. Acta 1017*, 251−272.
48. Reimers, J. R., and Hall, L. E. (1999) The Solvation of Acetonitrile, *J. Am. Chem. Soc. 121*, 3730−3744.
49. Warshel, A., Sharma, P. K., Kato, M., Xiang, Y., Liu, H., and Olsson, M. H. M. (2006) Electrostatic Basis for Enzyme Catalysis, *Chem. Rev. 106*, 3210−3235.
50. Fafarman, A. T., Webb, L. J., Chuang, J. I., and Boxer, S. G. (2006) Site-Specific Conversion of Cysteine Thiols into Thiocyanate Creates an IR Probe for Electric Fields in Proteins, *J. Am. Chem. Soc. 128*, 13356−13357.

BI701708U